physica status solidi a
www.pss-a.com

Optimization of Microwave Dielectric Properties of (100-X) $BaBi_4Ti_4O_{15}$ – (X)Nb_2O_5 Composites for Microwave

Paulo M. O. Silva, Roterdan F. Abreu, Francisco E. A. Nogueira, João P. C. do Nascimento, Daniel B. Freitas, Francisco F. do Carmo, Marcelo A. S. Silva, José A. Cruz, Rogério R. Pezarini, João Manuel R. S. Tavares, and Antônio S. B. Sombra*

This study focuses on experimental investigations and numerical simulations of microwave dielectric properties and dielectric resonator antenna behavior based on the $BaBi_4Ti_4O_{15}$ ceramic matrix. $BaBi_4Ti_4O_{15}$ is doped with niobium oxide (Nb_2O_5) in proportions of 2, 5, and 10%. The ceramic is obtained through the solid-state reaction method. The resulting structures and dielectric properties of the samples are analyzed using powder X-ray diffraction, Raman spectroscopy, and scanning electron microscopy to examine the crystalline phases present in the ceramics. The Hakki–Coleman method is used to clarify the properties of permittivity and dielectric loss. The temperature coefficients of the resonant frequency (τ_f) range from –396.95 to –181.44 ppm °C^{-1}. Experimental measurements of the dielectric resonators, serving as antennas, yielded results such as reflection coefficient, gain, efficiency, bandwidth, and input impedance. The simulations aligned well with experimental results, suggesting the potential application of this material as an antenna device in the microwave spectrum.

1. Introduction

Modern wireless communication and information systems heavily depend on radio-frequency waves, making wireless technology an integral part of contemporary life.[1,2] The rapid growth of fifth-generation (5G) communication applications, driven by new lifestyle demands, has created an urgent need for faster communications and higher data transmission capacity with wider coverage and lower signal latency.[3] These demands necessitate the development of novel materials for electronic circuits, including dielectrics, filters, oscillators, and other components that increasingly require miniaturization.[4–8]

Electroceramics serve a broad range of applications, encompassing magnetic, dielectric, ionically conductive, semiconducting, and superconducting ceramics. These materials are utilized in electronic devices as mobile phone applications, antennas for radar systems, wireless broadband networks, radio-frequency identification (RFID) devices, Bluetooth technology, satellite communications, and military technology.[9–11]

Within the group of electroceramics are ferroelectrics, which are materials that have excellent dielectric properties and are characterized by a low resonant frequency temperature coefficient, high permittivity, and spontaneous polarization, making them well-suited for various technological applications.[12–15] They also demonstrate high resistance to polarization fatigue, making them suitable for pressure sensors and non-volatile dynamic memory applications.[13,14]

There has been a marked increase in the production of these materials for wireless communication systems operating in the microwave range using dielectric resonator antennas (DRAs). DRAs offer the distinct advantages of lower conductive losses and greater variety in shapes and materials.[16] The increasing demand for smaller, more efficient, and cost-effective devices is paramount for electronic devices operating in the lower frequency band (below 1 GHz), the high-frequency band (1–6 GHz), and the very high-frequency band (greater than 6 GHz).

Many papers on microwave dielectric ceramics (MWDCs) applications have recently been published. For example, Zhou et al.[17] reported $Ce_2Zr_3(MoO_4)_9$–$(Mg_{1/3}Sb_{2/3})^{4+}$, calcined at 700 °C for 2 h, obtained permittivity $\varepsilon_r = 10.37$,

P. M. O. Silva, R. F. Abreu, F. E. A. Nogueira, J. P. C. do Nascimento, D. B. Freitas, F. F. do Carmo, M. A. S. Silva, A. S. B. Sombra
Telecommunication and Materials Science and Engineering of Laboratory (LOCEM) Physics Department
Federal University of Ceará (UFC)
Fortaleza, Ceará 60440-900, Brazil
E-mail: roterdan@alu.ufc.br

R. F. Abreu, F. E. A. Nogueira
Telecommunication Engineering Department
Federal University of Ceará (UFC)
Fortaleza, Ceará 60440-900, Brazil

J. P. C. do Nascimento
Federal Institute of Education, Science and Technology of Ceará
Fortaleza, Ceará 60055-172, Brazil

J. A. Cruz, R. R. Pezarini
Department of Environment
State University of Maringá
Umuarama, Paraná 87020-900, Brazil

J. Manuel R. S. Tavares
Mechanical Engineering Department
University of Porto
4200-465 Porto, Portugal

The ORCID identification number(s) for the author(s) of this article can be found under https://doi.org/10.1002/pssa.202400831.

DOI: 10.1002/pssa.202400831

$Q \times f = 71\,748$ GHz, and resonant frequency $\tau_f = -13.6$ ppm °C^{-1}. Alzakree et al.[18] reported $(Na_{0.5}Bi_{0.5})MoO_4$–$BaMoO_4$, solid-state, calcined at 550 °C for 4 h, obtained permittivity $\varepsilon_r = 19.02$, $Q \times f = 15\,164$ GHz, and $\tau_f = -0.2$ ppm °C^{-1}. Zhang et al.[19] reported $(MgTi_{0.95}Sn_{0.05}O_3$–$xCa_{0.8}Sr_{0.2}TiO_3)$, solid-state, calcined at 1200 °C for 5 h, obtained permittivity $\varepsilon_r = 20.4$, $Q \times f = 63\,770$ GHz, and $\tau_f = -1.8$ ppm °C^{-1} and MTS-0.06CST-Q with $\varepsilon_r = 18.4$, $Q \times f = 74\,740$ GHz, $\tau_f = -4.3$ ppm °C^{-1}. Bao et al.[20] reported $Nd_2(Zr_{1-x}Ti_x)_3(MoO_4)_9$, calcined at 700 °C for 2 h, obtained permittivity $\varepsilon_r = 10.94$, $Q \times f = 82\,525$ GHz, and $\tau_f = -12.99$ ppm °C^{-1}. Abreu et al.[21] reported $SrBi_2Nb_2O_9$–Bi_2O_3, solid-state, calcined at 900 °C for 2 h, obtained permittivity between $15.35 \leq \varepsilon_r \leq 153.90$, $2.40 \times 10^{-2} \leq \tan\ \delta \leq 1.86 \times 10^{-2}$, and $-322.46 \leq \tau_f \leq -235.02$ ppm °C^{-1}. Azevedo et al.[22] reported $LaFe_2O_3$–$CaTiO_3$, solid-state, calcined at 1000 °C for 4 h, obtained permittivity between $9.16 \leq \varepsilon_r \leq 9.04$, $0.85 \times 10^{-3} \leq \tan\ \delta \leq 2.10 \times 10^{-3}$, and $130.05 \leq \tau_f \leq -53.42$ ppm °C^{-1}. Tian et al.[23] reported $Pr_2(Zr_{1-x}Ti_x)_3(MoO_4)_9$, calcined at 700 °C for 2 h, obtained permittivity $\varepsilon_r = 10.72$, $Q \times f = 64\,200$ GHz, and $\tau_f = -13.0$ ppm °C^{-1}. Abreu et al.[24] reported $YNbO_4$–TiO_2, solid-state, calcined at 1200 °C for 4 h, obtained permittivity between $9.16 \leq \varepsilon_r \leq 153.90$, $2.40 \times 10^{-2} \leq \tan\ \delta \leq 1.86 \times 10^{-2}$, and $-322.46 \leq \tau_f \leq -235.02$ ppm °C^{-1}. Vasconcelos et al.[25] reported $ZnNb_2O_6$–$ZnTiNb_2O_8$, solid-state, calcined at 1050 °C for 4 h, obtained permittivity between $24.80 \leq \varepsilon_r \leq 26.19$, $1.32 \times 10^{-4} \leq \tan\ \delta \leq 0.72 \times 10^{-4}$, and $-97.64 \leq \tau_f \leq -84.51$ ppm °C^{-1}. Bao et al.[26] reported CaO–MoO_3–La_2O_3–$CaLa_2(MoO_4)_4$ and Ca_3MoO_6 calcined at 700 and 1100 °C, respectively, for 2 h, obtained permittivity $\varepsilon_r = 10.11$, $Q \times f = 75\,162$ GHz, and $\tau_f = -36.34$ ppm °C^{-1} for $CaLa_2(MoO_4)_4$ and $\varepsilon_r = 11.26$, $Q \times f = 23\,801$ GHz, and $\tau_f = -28.26$ ppm °C^{-1} for Ca_3MoO_6. Abreu et al.[27] reported $Ba_2TiSi_2O_8$–TiO_2, solid-state, calcined at 1100 °C for 6 h, obtained permittivity between $12.64 \leq \varepsilon_r \leq 21.84$, $1.69 \times 10^{-2} \leq \tan\ \delta \leq 0.31 \times 10^{-2}$, and $-37.98 \leq \tau_f \leq 21.03$ ppm °C^{-1}. Nogueira et al.[28] reported $CaMoO_4$–TiO_2, solid-state, calcined at 900 °C for 4 h, obtained permittivity between $1.28 \leq \varepsilon_r \leq 19.0$, $7.8 \times 10^{-4} \leq \tan\ \delta \leq 7.3 \times 10^{-4}$, and $-6.0 \leq \tau_f \leq 166.0$ ppm °C^{-1}. Tian et al.[29] reported Ge^{4+}-substituted cordierite $Mg_2Al_4(Si_{1-x}Ge_x)_5O_{18}$, calcined at 1350 °C for 2 h, obtained permittivity $\varepsilon_r = 4.90$, $Q \times f = 128\,200$ GHz, and $\tau_f = -21.01$ ppm °C^{-1}. Barros et al.[30] reported $ZnNb_2O_6$–$CaTiO_3$, solid-state, calcined at 1050 °C for 4 h, obtained permittivity between $22.45 \leq \varepsilon_r \leq 22.73$, $0.09 \times 10^{-3} \leq \tan\ \delta \leq 1.36 \times 10^{-3}$, and $-74.93 \leq \tau_f \leq -8.16$ ppm °C^{-1}. Sales et al.[31] reported $Mg_4Nb_2O_9$–TiO_2, solid-state, calcined at 1100 °C for 6 h, obtained permittivity between $13.95 \leq \varepsilon_r \leq 14.08$, $5.92 \times 10^{-4} \leq \tan\delta \leq 5.06 \times 10^{-4}$, and $-43.0 \leq \tau_f \leq -47.0$ ppm °C^{-1}.

Therefore due to its electric properties, $BaBi_4Ti_4O_{15}$ (BBT) is a promising candidate for applications in electronic devices operating in the microwave range.[14,15] BBT is a dielectric, ferroelectric, and piezoelectric ceramic belonging to the Aurivillius family, formed by intercalated layers of bismuth block and pseudo-perovskite. BBT has a perovskite structure with a tetragonal structure and space group (Laue group) I4/mm, with a Curie temperature ranging from 390 to 440 °C. Due to its low sintering temperature, this ceramic is considered a low-temperature co-fired ceramic material.[6,7]

Thus, aiming to improve the electrical properties and thermal stability of the $BaBi_4Ti_4O_{15}$ ceramic matrix, niobium oxide (Nb_2O_5) was selected as an additive in the new composites. Nb_2O_5 has several technological applications across a wide frequency range from microwave to radio frequencies.[32] It presents an orthorhombic phase at temperatures below 900 °C, changing its phase only when subjected to temperatures above 1000 °C.[33]

Structural characterization of the BBT–Nb_2O_5 composites was conducted using X-ray diffraction (XRD). Additionally, the dielectric properties within the microwave region (MW) were explored, and the performance of these materials as DRAs was evaluated through numerical simulations. The analyzed ceramics emerged as compelling candidates for applications in devices operating in the S-band.

2. Experimental Section

2.1. Synthesis of $BaBi_4Ti_4O_{15}$ Perovskite

$BaBi_4Ti_4O_{15}$ ceramic was prepared using the conventional ceramic method, where precursor oxides BaO (99%, Aldrich), Bi_2O_3 (99.9%, Aldrich), and TiO_2 (99.9%, Vetec) were ground for 6 h at 360 rpm using the Fritsch Pulverisette 5 mill. The powder was calcined in a resistive oven at 850 °C for 3 h.

The composites were fabricated by simple mixing of Nb_2O_5 (99%, Aldrich) with BBT, with Nb_2O_5 concentrations varying from 0, 2, 5, and 10 wt%, and were designated BBT, BBTNb2, BBTNb5, and BBTNb10, respectively. Samples were compacted via uniaxial pressure of 12 MPa in the bulk format, using 5% polyvinyl alcohol (PVA) as a binder, and were sintered at 950 °C for 3 h in air.

2.2. X-Ray Diffraction

The powder X-ray diffraction (PXRD) patterns were recorded at room temperature (300 K) using an X'Pert MPD (PANalytical) diffractometer. The X-ray tube emitted CoK_∞ radiation ($K_{\infty 1}$: 1.788965 Å, $K_{\infty 2}$: 1.792850 Å) and operated at 40 kV and 30 mA. Diffraction patterns were acquired with Bragg–Brentano geometry in continuous mode at a scan speed of 1°/min over an angular range of $20° \leq 2\theta \leq 80°$. The phases in BBT and BBT–Nb_2O_5 ceramics were identified during calcination and sintering using diffraction peak analysis. The Rietveld refinement method was effectively employed to determine the quantitative phase abundances in the sintered samples.

2.3. Scanning Electron Microscopy

The microstructures of BBT samples were examined. Micrographs of pellet samples were captured at various magnifications employing a scanning electron microscope (SEM, VEGA II XMU) at room temperature. The objective was to discern the densification of BBT with the inclusion of Nb_2O_5 and to characterize the morphology of the grains.

2.4. Raman Spectroscopy

A high-resolution LabRam HR Horiba 800 spectrometer was used to obtain the active Raman spectrum of BBT and additions. The instrument is equipped with a CCD detector and a grating of 1800 lines mm^{-1}. A 785 nm infrared laser was used as the excitation source, and the beam was focused onto the sample using a 100×/0.90 long working distance microscope objective.

2.5. Dielectric Measurements at Microwave Frequencies

The dielectric properties at microwave frequencies were examined using the Hakki–Coleman technique,[34,35] which utilizes the resonant TE_{011} mode. An Agilent N5230C network analyzer was employed for the measurements. The dielectric permittivity (ε_r) and dielectric loss (tan δ) were determined from the resonant frequency of the TE_{011} mode at room temperature. The Li et al.[36] method was used to measure the resonant frequency temperature coefficient (τ_f). The τ_f value can be calculated using Equation (1):

$$\tau_f = \frac{1}{f_0} \cdot \frac{\Delta f}{\Delta T} \cdot 10^6 \ ppm.°C^{-1} \tag{1}$$

where f_0 is the resonant frequency of the $HE_{011\delta}$ mode measured at 25 °C, and df_0 and dT are the variations in resonant frequency and temperature (25–85 °C), respectively.

2.6. Resonator Configuration Employing in the Numerical Simulation

The measurements were performed using the transmission/reflection network analyzer, Agilent N5230C. The dielectric resonator antennas (DRAs) were stimulated by a wire antenna positioned above a ground plane. The configuration of the cylindrical DRAs is depicted in **Figure 1**. The experimental setup consisted of a ceramic cylinder with a height (h), diameter (D), and radius (a). The sample was situated on a copper ground plane (355 × 300 × 2.14 mm) and was placed as close as possible to the probe, which was connected to the analyzer via a 50 Ω SMA connector.

In this configuration, the dominant mode of this dielectric resonator is the $HE_{11\delta}$, where the characteristics of this mode, such as resonance frequency ($f_{HE11\delta}$) and quality factor (Q), can be approximated using the following equations (see Supporting Information):[37]

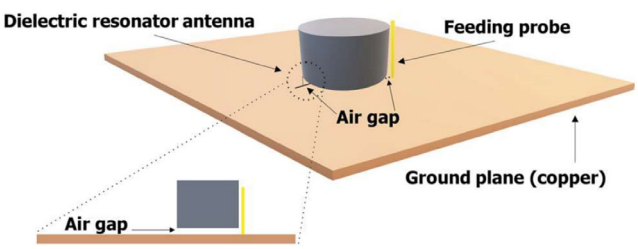

Figure 1. Schematic illustration of the setup used for DRA measurements.

$$f(HE_{11\delta}) = \frac{6.324c}{2\pi a\sqrt{\varepsilon_r + 2}}\left(0.27 + 0.36\frac{a}{2L} + 0.02\left(\frac{a}{2L}\right)^2\right) \tag{2}$$

and,

$$Q = 0.01007(\varepsilon_r^{1.3})\frac{a}{L}\left\{1 + 100\exp\left[-2.05\left(\frac{a}{2L} - 0.0125\left(\frac{a}{L}\right)^2\right)\right]\right\} \tag{3}$$

The far-field parameters were obtained using Ansoft high-frequency structure simulator (HFSS). HFSS uses the finite element method to simulate electromagnetic fields and design high-frequency components.[21,27,37] The effect of an air gap around the coaxial probe exciting a cylindrical dielectric resonator antenna was also considered.[38,39] In this way, the parameters obtained included directivity, gain, and a radiation pattern.

2.7. *S* Parameter

The feed port's input impedance ($Z = R + jX$) produces a frequency response due to the resonant behavior of each mode of the highly resonant structure of the DRA. At the resonant frequency f_0, the resistance R reaches its maximum and the reactance X becomes zero, as shown in Figure 1 illustrating the reflection coefficient (S_{11}). It is important to note that the deviation of resonant frequencies from the minimum of the reflection coefficient S_{11} is determined by the equation relating to Z:

$$S_{11} = \frac{z - 1}{z + 1} \tag{4}$$

with $z = Z/R_C$, where R_C is the characteristic impedance of the feeder. Equation (4) clearly shows that S_{11} depends on R_C: using $R_C = 50\,\Omega$ feeder, it can be seen that the power transmission to the antenna is high ($S_{11} \neq 0$) at the resonant frequency of the DRA.

3. Results and Discussion

3.1. X-Ray Diffraction

Figure 2 shows the refinements of the BBT matrix and composites. All peaks of BBT align precisely with the ICSD pattern, with no additional peaks observed from other phases. To corroborate the structure of the chosen tetragonal BBT, quantitative phase analysis was executed using the Rietveld refinement method[32,40,41] with GSAS/EXPGUI software.[42]

The study confirmed the crystal structure, revealing lattice parameters: $a = 3.856$ Å, $b = 3.856$ Å, and $c = 41.958$ Å; with angles, $a = b = c = 90°$, and a calculated $\rho = 7.48\ g\,cm^{-3}$ and unit cell volume equal to 623.166 $Å^3$ for the pure phase. **Table 1** details the impurity phases found using the Rietveld refinement performed on the BBT–Nb_2O_5 composites to determine the crystalline phases present (see **Figure 3**). It was observed that BBT and Nb_2O_5 reacted, leading to the formation of the $Bi_{1.74}Ti_2O_{6.624}$ phase. Bismuth titanates, along with the pyrochlore phase associated with the cubic $Bi_{1.74}Ti_2O_{6.624}$ phase [PDF 089-4732], contain mixtures of the tetragonal $Bi_4Ti_3O_{12}$ [PDF 047-0398] and tetragonal Bi_2O_3 [PDF 071-0465] phases.[43]

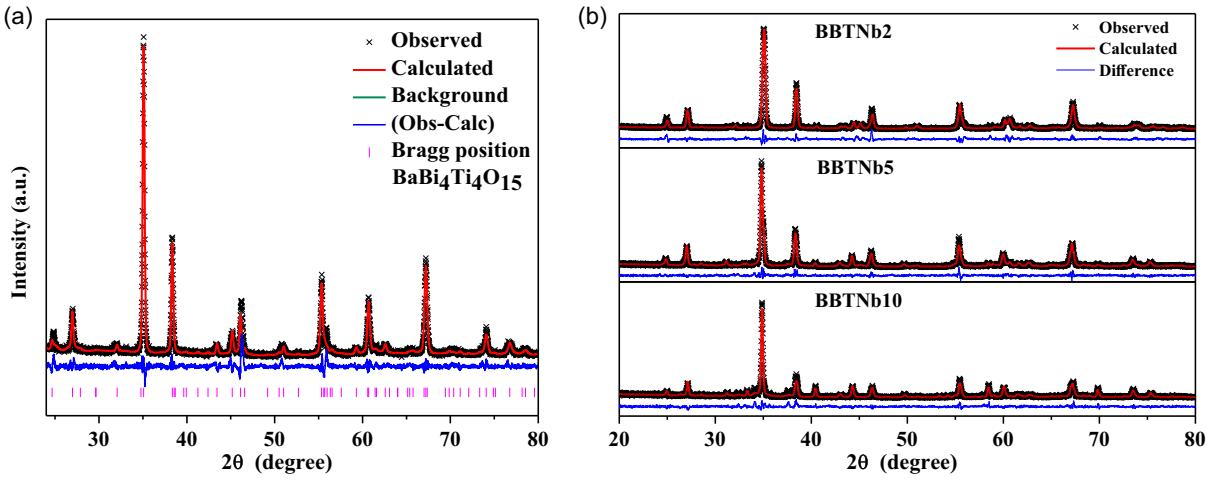

Figure 2. a) Rietveld refinement for the BBT matrix and b) composites.

Table 1. Parameters from Rietveld refinement for BBT–Nb_2O_5 system.

Samples	Parameters			Mass fraction [%]		
	χ^2	R_{wp} [%]	R_{Bragg} [%]	BBT	Nb_2O_5	$Bi_{1.74}Ti_2O_{6.624}$ (pyrochlore)
BBT	1.28	13.83	8.36	100	–	–
BBTNb2	1.58	13.72	14.40	78.12	–	21.82
BBTNb5	1.47	14.79	14.60	56.28	–	34.03
BBTNb10	1.49	14.62	11.20	19.09	31.38	49.53

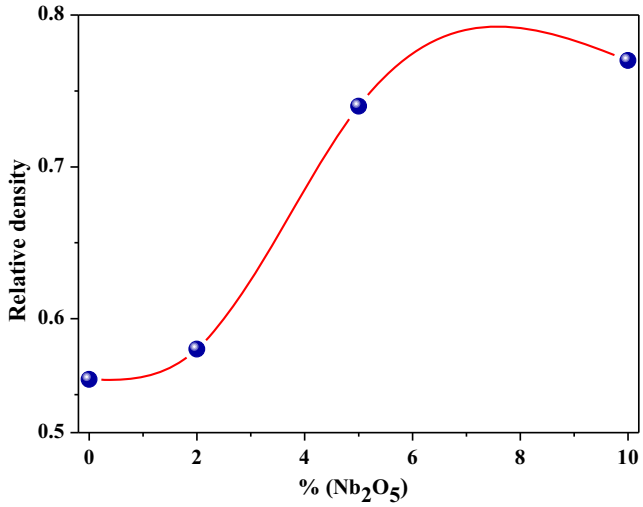

Figure 3. Relative density variation % Nb_2O_5.

Makovec et al. and Pribosic et al. confirmed the presence of the $BaBi_4Ti_4O_{15}$ phases and the pyrochlore phase when doped with 5% Nb_2O_5. Additionally, when doped with 10% Nb_2O_5, the three phases observed were the $BaBi_4Ti_4O_{15}$ matrix, the pyrochlore phase, and Nb_2O_5.[44,45]

Table 1 presents the statistical parameter values derived from the Rietveld refinement and the percentage of phases in the composites. The parameters, including reduced chi-square (χ^2), weighted-profile reliability factor (R_{wp}), and Bragg intensity reliability factor (R_{Bragg}), demonstrate a robust agreement between the observed and calculated XRD patterns. This affirmation underscores the reliability of the accomplished refinement.

The experimental density for all samples was determined through pycnometry. The theoretical densities of BBT and Nb_2O_5 were derived via Rietveld refinement, yielding $\rho = 7.48\,g\,cm^{-3}$ for BBT and $\rho = 4.36\,g\,cm^{-3}$ for Nb_2O_5. The results for both absolute density (ρ) and relative density (ρ_r) are detailed in **Table 2** and depicted in Figure 3. Subsequently, the ρ_r was calculated according to Equation (5):

$$\rho_r = \frac{\rho_e}{\rho_t} \tag{5}$$

where ρ_e and ρ_t are the experimental and theoretical densities, respectively. It is noteworthy that these ρ_r values are lower than the corresponding theoretical densities. Specifically, the BBT ceramic's relative density is notably low compared to reported literature values for the same phase under different sintering conditions.[13–15] However, the BBTNb2, BBTNb5, and BBTNb10 ceramics exhibited a substantial increase in densification during the process.

Table 2. Relative density values of BBT–Nb_2O_5 composites.

	Density [$g\,cm^{-3}$]		
Samples	Theoretical	Experimental	Relative [%]
BBT	7.48	4.17	55.74
BBTNb2	7.17	4.29	59.83
BBTNb5	6.38	5.38	84.32
BBTNb10	6.36	5.59	87.89

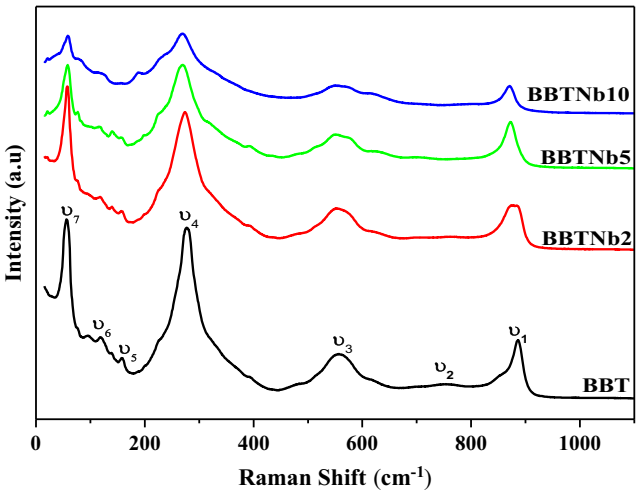

Figure 4. Comparison of the Raman modes for the BTT, BTTNb2, BTTNb5, and BTTNb15 at room temperature.

3.2. Raman Spectroscopy

To elucidate the vibrational modes of the crystalline phases, Raman spectroscopy was employed to analyze the ceramics. As depicted in **Figure 4**, the Raman spectra exhibit seven distinct peaks within the 0–1000 cm^{-1} range, attributed to the BBT and Nb_2O_5 phases. These findings align well with reported data.[46–48] The Raman spectrum of $BaBi_4Ti_4O_{15}$ reveals three peaks around 160, 280, and 880 cm^{-1} at room temperature. Literature indicates that Nb_2O_5 modes closely resembling the BBT phase spectrum are observed at 120, 555, 755, and 900 cm^{-1}.[33] A prominent peak at 886.86 cm^{-1} corresponds to the A_{1g} (ν_1) mode. Additionally, strong peaks at 556.96, 277.42, and 57.63 cm^{-1} are clearly visible and align with the modes (ν_3), (ν_4), and (ν_7), respectively. The peaks 753.83 cm^{-1} (B_{1g} (ν_2)) and the less intense 118.23 cm^{-1} (A_{1g} (ν_6)) are associated with the vibrational modes of the Nb_2O_5 phase. The vibrational modes corresponding to the BBT phase are represented by peaks at 886.86 cm^{-1} (A_{1g} (ν_1)), 556.96 cm^{-1} (A_{1g} (ν_3)), 277.42 cm^{-1} (B_{2g}/B_{3g} (ν_4)), and 158.10 cm^{-1} (A_{1g} (ν_5)).[48] Moreover, the high-intensity ν_1 peak at 888.86 cm^{-1} is attributed to the BBT and Nb_2O_5 phases. These results unequivocally corroborate the findings from the XRD measurements.

In the case of $BaBi_4Ti_4O_{15}$ ceramics doped with Nb_2O_5, the decrease in the intensity of the Raman spectrum occurs due to the incorporation of the Nb^{5+} ion into the Ti^{4+} ion site in the crystal lattice of the BBT crystals, generating an increase in the concentration of barium (Ba^{2+}) and a decrease in the concentration of bismuth (Bi^{3+}). Since Nb^{5+} has an ionic radius of 0.64 Å, it is incorporated exclusively into the Ti^{4+} site, which has an ionic radius of 0.61 Å. However, Nb^{5+} cannot substitute for Ba^{2+} (1.35 Å) or Bi^{3+} (1.17 Å) because its ionic radius is smaller. This fact is attributed to the structural disorder associated with chemical changes and compositional fluctuations.

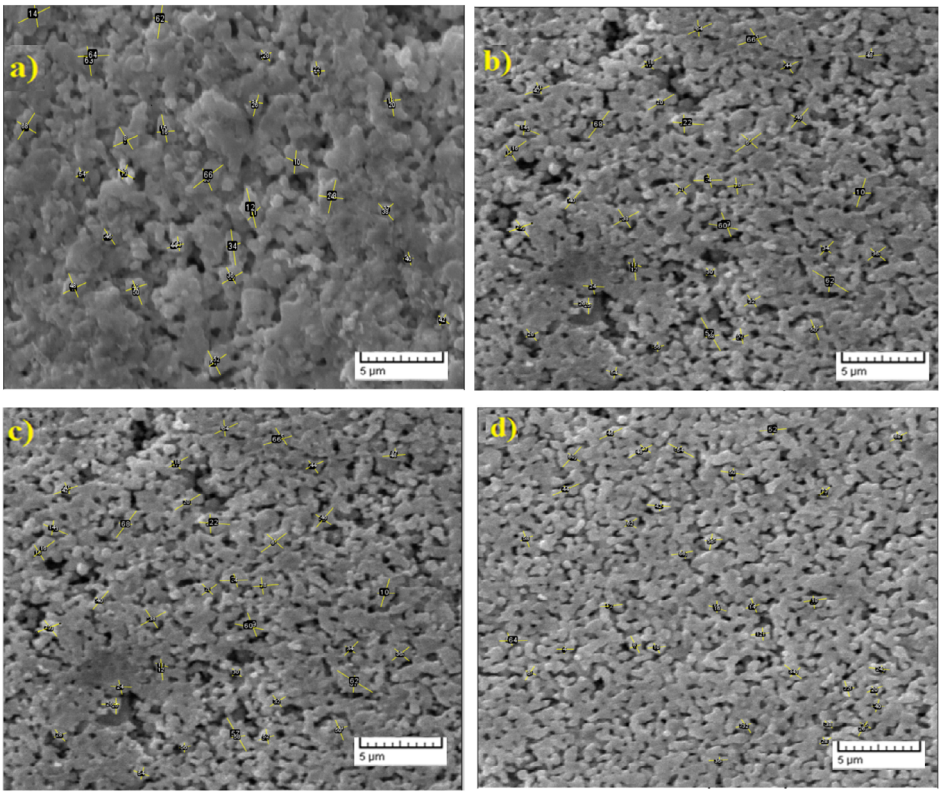

Figure 5. SEM micrographs at room temperature with a magnification factor of 5000× for: a) BBT, b) BBTNb2, c) BBTNb5, and d) BBTNb10.

These fluctuations give rise to microdomains with different levels of structural distortion that become visible with the increase in the concentration of Nb_2O_5.[49]

3.3. Scanning Electron Microscopy

The microstructure of the surfaces was investigated through SEM analysis, as presented in **Figure 5**. Micrographs captured at a magnification of 5000× revealed a consistent microstructure across the sintered BBT, BBTNb2, BBTNb5, and BBTNb10 ceramics. These samples exhibited a combination of grains and pores in specific regions, accompanied by a nonuniform distribution of grain sizes. In this way, the addition of oxides is beneficial and favors grain packing.

Figure 5a shows a significant amount of space in most areas with particulate structures that did not have a clearly defined shape. This was confirmed by a low density of ≈56%. However, most areas exhibited well-defined grains, grain boundaries, and minimal void space compared to the BBT ceramic, as illustrated in Figure 5b–d. These findings indicate that adding niobium oxide to the BBTNb2, BBTNb5, and BBTNb10 ceramics substantially improved the densification of the material.

The software ImageJ was used to analyze the average grain size. A conversion scale between the number of pixels in the image and the actual size was assigned through the software, and then, on average, 35 distinct and random grains distributed throughout the entire image (SEM) were selected. A grain size of around 1.3 μm was observed in the pure sample. The grain size of the doped samples was between 1 and 1.3 μm. The grain size of the BBT–Nb_2O_5 specimens became more homogeneous with the increase in niobium content, favoring better packing of the grains and improving the density of the Nb-doped samples.

The EDS spectrum (see **Figure 6**) confirmed the presence of anionic and cationic elements (Ba, Bi, Ti, O, and Nb ions).

Table 3. Weight percent and atomic percent of elements obtained from EDS analysis.

Sample		Ba	Bi	Ti	O	Nb
$BaBi_4Ti_4O_{15}$	Weight %	7.44	60.29	16.17	16.09	–
	Atomic %	3.21	17.11	20.03	59.65	–
BBTNb2	Weight %	6.98	71.62	19.32	–	2.10
	Atomic %	6.21	41.83	49.20	–	2.76
BBTNb5	Weight %	9.63	67,08	19.32	–	3.97
	Atomic %	8.37	38.33	48.19	–	5.11
BBTNb10	Weight %	8.59	60.74	23.89	–	6.78
	Atomic %	6.76	31.42	53.94	–	7.89

Table 4. Dielectric properties in the microwave region obtained for all samples evaluated.

Samples	a [mm]	h [mm]	f_0 [GHz]	ε_r	tanδ [10^{-2}]	τ_f [ppm °C^{-1}]	$Q \times f$ [GHz]
BBT	8.84	8.79	4.64	52.40	8.35	−420.31	91.63
BBTNb2	9.20	9.34	4.77	50.37	6.38	−396.95	86.27
BBTNb5	9.19	9.16	4.33	51.40	4.56	−302.18	142.33
BBTNb10	9.20	9.40	4.09	52.65	4.59	−181.43	127.65

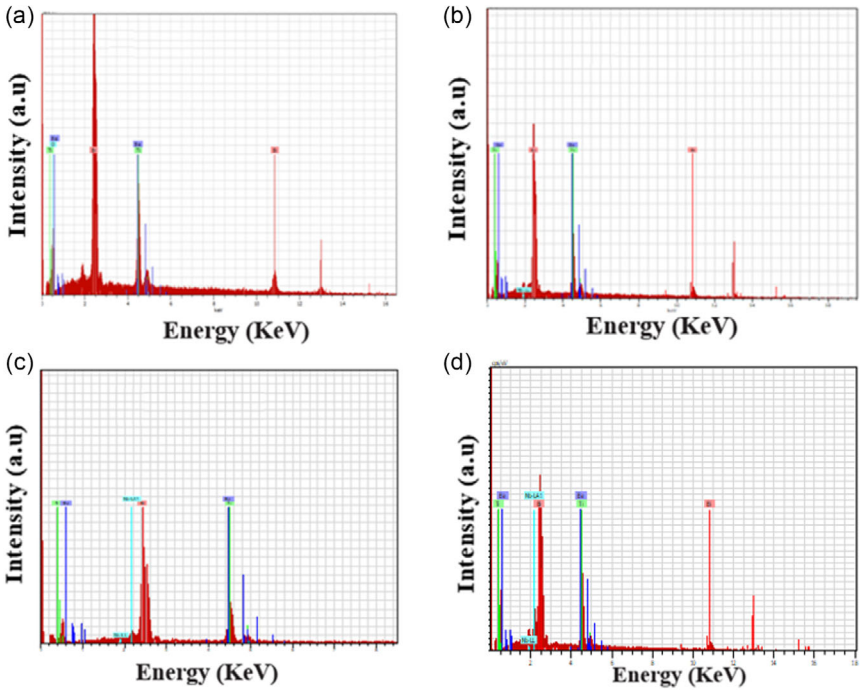

Figure 6. Elemental mapping from EDS for all samples. a) $BaBi_4Ti_4O_{15}$ (BBT); b) BBTNb2; c) BBTNb5; d) BBTNb10.

Table 3 presents the elemental weights provided by the EDS analysis. The recorded EDS spectra show that all the elements of the studied samples are present. These results corroborate the XRD and Rietveld refinement analyses presented earlier.

3.4. Dielectric Measurements at Microwave Frequency

The dielectric properties within the microwave range of the BBT–Nb_2O_5 systems were assessed through the Hakki–Coleman technique. As indicated in **Table 4** and illustrated in **Figure 7**a, all

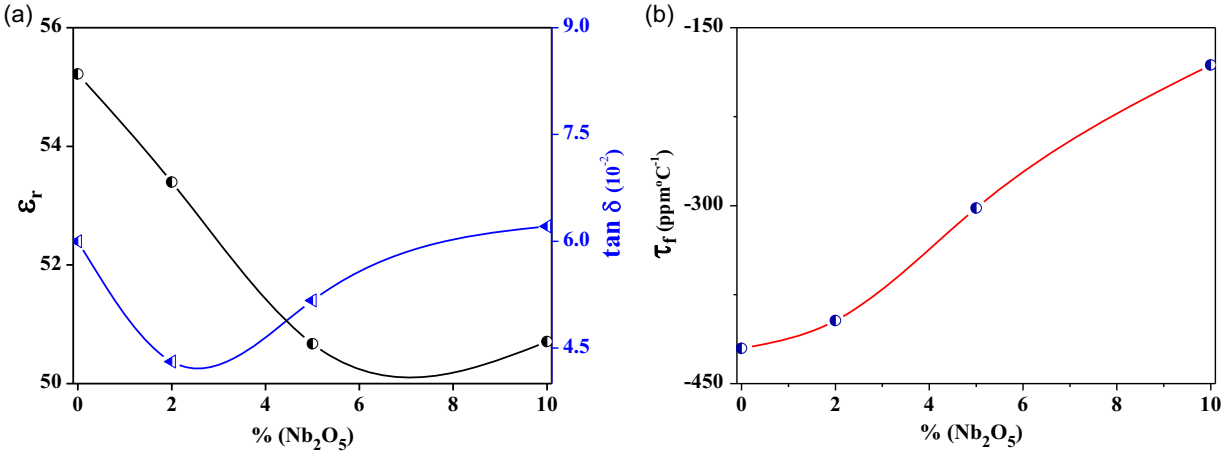

Figure 7. a) Dielectric permittivity (ε_r) and dielectric losses (tan δ) and b) resonant frequency temperature coefficient (τ_f) variation with Nb_2O_5.

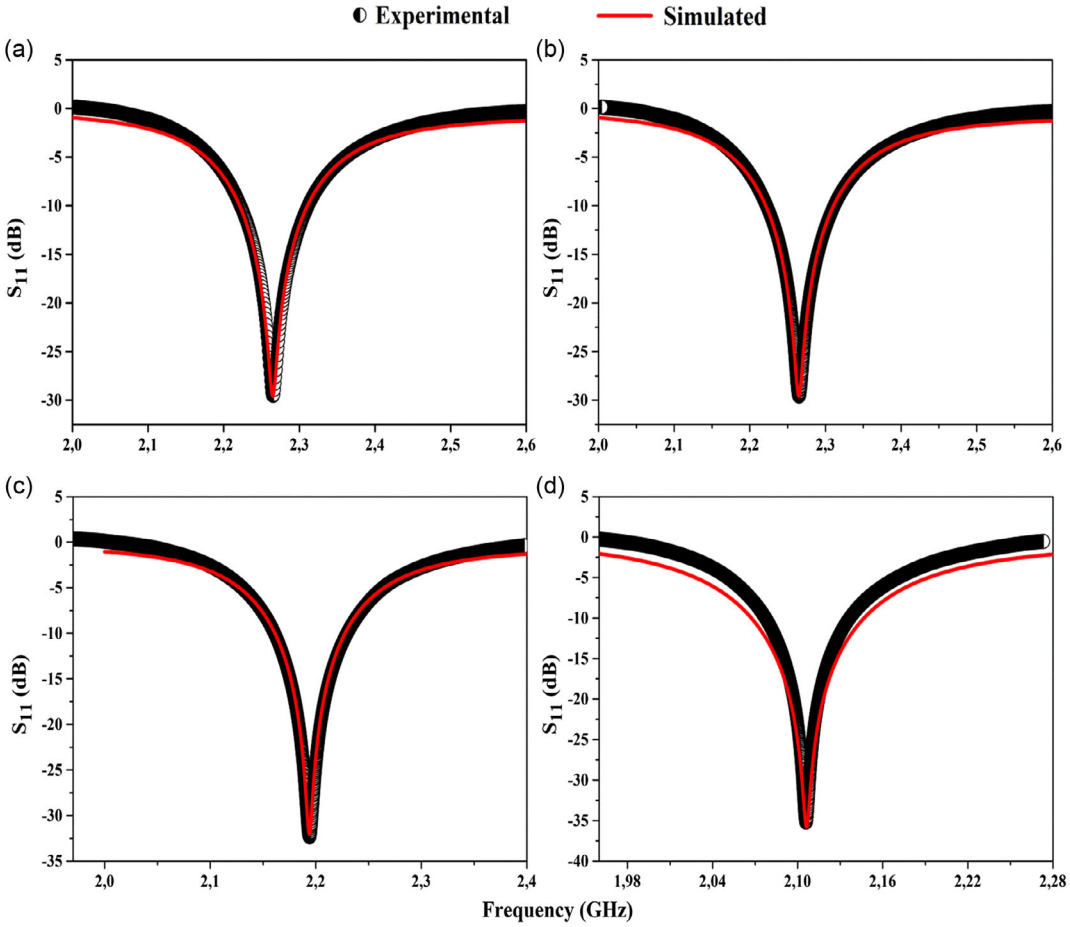

Figure 8. Experimental and theoretical HFSS reflection coefficient (S_{11}) from a) BBT, b) BBTNb2, c) BBTNb5, and d) BBTNb10.

Table 5. Experimental and simulated values of resonant frequency (f_r), reflection coefficient (S_{11}), and percent bandwidth (% BW) for samples.

Parameter	BBT	BBTNb2	BBTNb5	BBTNb10
$f_{experimental}$ [GHz]	2.26	2.16	2.19	2.10
$f_{simulated}$ [GHz]	2.26	2.16	2.19	2.10
Error [%]	0.00	0.00	0.00	0.00
$Z_{experimental}$ [Ω]	49.13	52.61	50.11	54.77
$Z_{simulated}$ [Ω]	48.34	52.79	50.84	54.50
Error [%]	1.61	0.34	1.46	0.49
$S_{11experimental}$ [dB]	−29.58	−33.03	−32.35	−35.20
$S_{11simulated}$ [dB]	−29.58	−33.53	−32.01	−35.72
Error [%]	0.00	1.51	1.05	1.47

samples exhibited resonant frequencies (f_0) ranging from 4.09 to 4.77 GHz. Notably, the highest dielectric permittivity was observed in the BBTNb10 sample ($\varepsilon_r = 52.65$), while concurrently displaying a lower dielectric loss (tan $\delta = 4.56 \times 10^{-2}$). This enhancement in ε_r is attributed to the increased density resulting from adding Nb_2O_5, as detailed in Table 4.[50,51]

In particular, the sintering temperature employed in this study was 950 °C, a notable departure from the literature where sintering temperatures typically exceed 1000 °C. The dielectric properties analyzed in this study showed ε_r lower than those reported in the literature due to the influence of the lower densification acquired (Table 2). A higher sintering temperature promotes higher densification, contributing to grain growth. Grain size is a determining factor for the electrical properties of the material, that is, the larger the grains, the smaller the vacancies within the sample, improving its dielectric properties, and consequently ε_r.[52,53]

The lower density is the result of our choice to study BBT at low sintering temperatures (<1000 °C), which opens the possibility of using this material in low-temperature co-fired ceramics (LTCC).

Regarding dielectric losses (tan δ), no substantial variation was noted, with all materials exhibiting tan δ values on the order of 10^{-2}. This consistency arises from the similar tangent loss values of the BBT and Nb_2O_5 phases (tan $\delta_{Nb2O5} = 3.65 \times 10^{-2}$).[54] Thermal stability analysis, conducted using the Li et al. method,[36] revealed a negative temperature coefficient of the resonant frequency (τ_f) for all samples, as depicted in **Figure 8**b and detailed in Table 4.

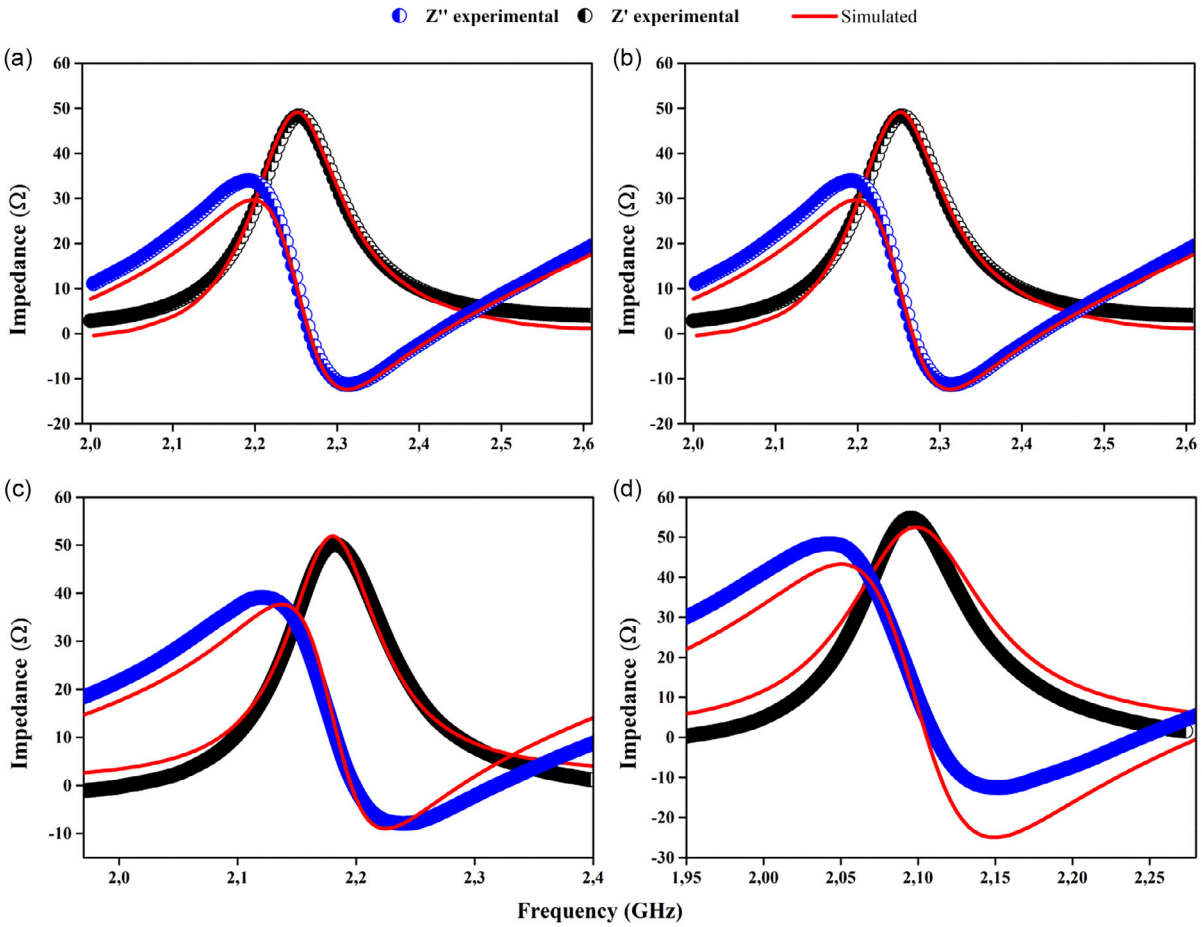

Figure 9. Real and imaginary impedances (experimental and simulated) for a) BBT, b) BBTNb2, c) BBTNb5, and d) BBTNb10.

The BBTNb10 sample exhibited a lower τ_f value (–181.43 ppm °C^{-1}), which is attributed to the negative τ_f values inherent in both the BBT and Nb_2O_5 phases.[55,56] Extensive efforts have been undertaken to empirically control τ_f values in dielectric materials, forming solid solutions and homogeneous phases by combining two or more components with both negative and positive values. This pursuit aims to achieve coefficients close to zero, a crucial requirement for commercial microwave applications.[57,58]

3.5. Numerical Simulation of the BBT–Nb_2O_5 Composites

Numerical simulations were conducted using Ansoft (HFSS) high-frequency structure simulator software to analyze the behavior of BBT–Nb_2O_5 composites functioning as DRAs. Figure 8a–d show the experimental and simulated reflection coefficient (S_{11}) for the materials, where the experimental and simulated S_{11} profiles are well adjusted. As presented in **Table 5**, the error in simulated frequency is less than 0.02% for all samples. For the value of the reflection coefficient, the error is higher for BBTNb2 (1.51%), whereas BBTNb5 and BBTNb10 presented errors close to 1.05 and 1.47%, respectively. Moreover, all systems analyzed presented $S_{11} < -10$ dB, demonstrating that the ceramics analyzed can operate as an antenna.[11,59,60] The resonance frequency of the samples was between 2 and 4 GHz, and according to the classification given by the Institute of Electrical and Electronic Engineers (IEEE), these composites can operate as S-band electronic devices.

The comparison between real (Z') and imaginary (Z'') impedances was also performed to demonstrate that the simulation performed for materials is reliable (**Figure 9**a–d). Z' and Z'' demonstrated a good approximation between simulated and experimental results, while the difference observed could be explained by the fact that the theoretical model does not consider the ground plane imperfections of the DRA.

Figure 10a–d present the simulated radiation pattern of gain, describing how the DRA radiated into free space at θ and ϕ angles. The analyzed samples present quite similar radiation patterns. The simulated radiation patterns for the E-plane ($\phi = 0°$) and H-plane ($\phi = 90°$) show that the symmetry of the lobes demonstrates a good coupling. The profile demonstrates a typical diagram of a cylindrical DRA, with the maximum radiation at $\theta = 0°$, i.e., at the top of the cylinder.[55,56]

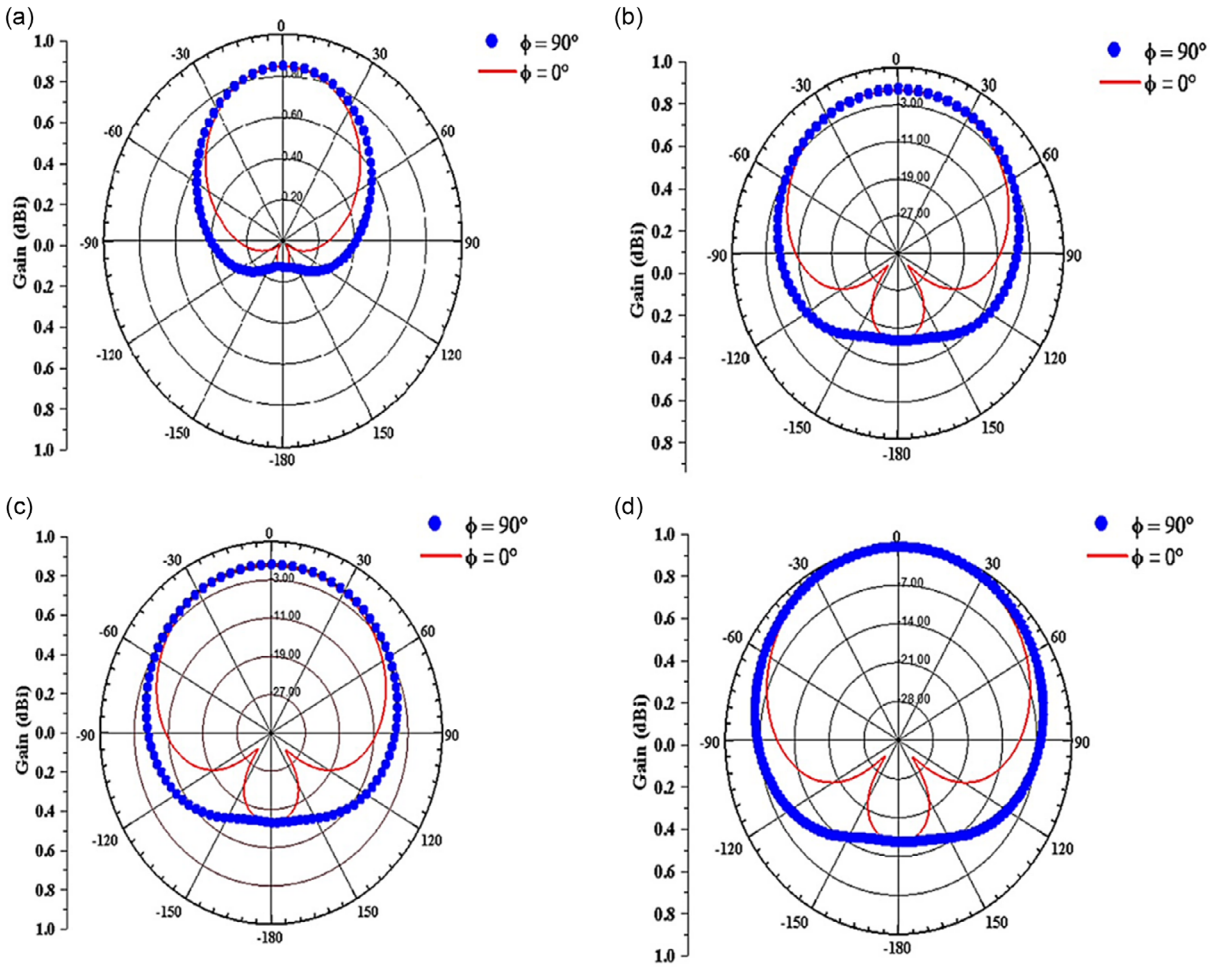

Figure 10. Simulated radiation pattern of E_θ ($\phi = 0°$), E_θ ($\phi = 90°$), and E_ϕ ($\theta = 0°$) of a) BBT, b) BBTNb2, c) BBTNb5, and d) BBTNb10.

Table 6. DRA operating parameters determined by the simulation in the HFSS.

Samples[a)]	D [mm]	H [mm]	Direc. [dBi]	Gain [dBi]	Γ	Γpwr	Tpwr	BW_{Exp} [MHz]
BBT	15.910	7.60	3.45	1.12	0.0331	0.00110	0.9988	89.48
BBTNb2	17.443	8.44	3.30	1.12	0.0223	0.00049	0.9995	89.43
BBTNb5	17.256	8.03	3.39	1.41	0.0241	0.00058	0.9994	68.93
BBTNb10	17.045	8.49	3.21	1.15	0.0173	0.00030	0.9996	59.45

[a)]Diameter; Height; Directivity; Gain; Reflection coefficient (Γ); Energy reflection coefficient (Γpwr); Energy transmission coefficient (Tpwr); Bandwidth (BW_{Exp}).

The far-field parameters for BBT–Nb_2O_5 composites are detailed in Table 5, showcasing directivity exceeding 3.00 dBi and bandwidth ranging from 59.45 to 89.48 MHz. These results suggest that the evaluated materials hold significant potential for applications in electronic devices operating in the S-band, including Wi-Fi devices and satellite communication transmissions.[57–60]

The impact of dielectric loss on the radiation characteristics of the samples, when functioning as DRAs or cylindrical antennas, is noteworthy. The enhanced densification resulting from niobium oxide doping contributed to increased permittivity and reduced dielectric loss. In this context, niobium oxide doping enabled the exploration of the influence of different addition percentages on key parameters such as bandwidth, efficiency, and antenna gain. It is worth noting that these characteristics can be further optimized by modifying the symmetry or dimensions of the DRA. **Table 6** presents the directivity, gain, reflection coefficient (Γ), energy reflection coefficient (Γpwr), and energy transmission coefficient (Tpwr) of the analyzed DRAs.

Furthermore, it is possible to observe that the samples demonstrated directivity below 3.50 dBi and gain less than 1.50 dBi, with the bandwidth decreasing throughout the series. However, an Γ value close to zero in all samples suggests that most of the energy was being transmitted and that some of this energy was lost through reflection with the energy reflection coefficient (Γpwr) indicating how much energy was lost by reflection. It is observed that all samples have values very close to zero, between 10^{-3} and 10^{-4}. The power transmission coefficient (Tpwr) indicates how much power is transmitted as a function of transmission line mismatch, that is, the closer this value is to 1, the higher the energy transmission and the lower the loss due to impedance mismatch. All samples show good results with values very close to 1.[58–62]

4. Conclusion

This study delved into the microwave properties of the BBT–Nb_2O_5 composites. XRD was used to analyze the materials, and it was observed that the addition did not result in the formation of new phases. Raman spectroscopy revealed peaks 886.86 cm^{-1} (A_{1g} (ν_1)), 556.96 cm^{-1} (A_{1g} (ν_3)), 277.42 cm^{-1} (B_{2g}/B_{3g} (ν_4)), and 158.10 cm^{-1} (A_{1g} (ν_5)) corresponding to the BBT phase, while the peaks 753.83 cm^{-1} (B_{1g} (ν_2)) and the less intense 118.23 cm^{-1} (A_{1g} (ν_6)) are associated with the vibrational modes of the Nb_2O_5 phase. A decrease in the intensity of the Raman spectrum was also observed due to the incorporation of the $Nb5^+$ ion into the $Ti4^+$ ion site in the crystal lattice of BBT crystals, this fact is attributed to the structural disorder associated with chemical changes and compositional fluctuations. The microstructure of the surfaces was investigated through SEM analysis. Micrographs revealed a consistent microstructure across the sintered BBT, BBTNb2, BBTNb5, and BBTNb10 ceramics. The samples showed a non-uniform distribution for grain sizes. The EDS spectrum confirmed the presence of anionic and cationic elements (Ba, Bi, Ti, O, and Nb ions). Analysis of dielectric measurements indicated that the inclusion of Nb_2O_5 led to an increase in permittivity and a reduction in dielectric loss tangent. The dielectric properties analyzed in this work revealed ε_r variations between 50.37 and 52.65, with tan δ values ranging from 6.01×10^{-2} to 4.59×10^{-2}, whereas the addition of Nb_2O_5 resulted in the τ_f of BBT closer to zero. Numerical simulations were employed to evaluate the performance of the investigated composites as a DRA. The experimental and simulated curves exhibited a robust alignment, with all samples displaying reflection coefficient (S_{11}) values lower than –10 dB, indicating their suitability for operation as antennas. Furthermore, the far-field parameters of the ceramics demonstrated a bandwidth ranging from 59.45 to 89.48 MHz, showcasing the potential applicability of these materials in electronic devices operating within the S-band.

Supporting Information

Supporting Information is available from the Wiley Online Library or from the author.

Acknowledgements

This work was partly sponsored by the Brazilian Research Agencies CNPq-Conselho Nacional de Desenvolvimento Científico e Tecnológico [grant INCT NANO(BIO)SIMES]; CAPES- Coordenação de Aperfeiçoamento de Pessoal de Ensino Superior [grant project PNPD]; FINEP-Financiadora de Estudos e Projetos [grant INFRAPESQ-11 and INFRAPESQ-12]; U. S. Air Force Office of Scientific Research [(AFOSR) (FA9550-16-1-0127)].

Conflict of Interest

The authors declare no conflict of interest.

Author Contributions

Paulo M. O. Silva: conceptualization, investigation, writing—original draft; **Roterdan F. Abreu**, **Francisco E. A. Nogueira**: writing—original draft, data curation; **João P. C. do Nascimento**: methodology; **Roterdan F. Abreu**, **Francisco E. A. Nogueira**: software; **Francisco F. do Carmo**: validation: **Marcelo A. S. Silva**: writing—review; **José A. Cruz**: investigation; **Rogério R. Pezarini**: software; **Daniel B. Freitas**: visualization and formal analysis; **Roterdan F. Abreu**: writing—review and editing; **João Manuel R. S. Tavares**: project administration, supervision; **Antônio S. B. Sombra**: funding acquisition, resources.

Data Availability Statement

The data that support the findings of this study are available in the supplementary material of this article.

Keywords

$BaBi_4Ti_4O_{15}$–Nb_2O_5, dielectric resonator antenna, microwave, simulation

Received: October 17, 2024
Revised: January 27, 2025
Published online: February 12, 2025

[1] J. M. Jornet, E. W. Knightly, D. M. Mittleman, *Nat. Commun.* **2023**, *14*, 841.
[2] M. Islam, S. Jin, *Adv. Wireless Commun. Networks* **2019**, *5*, 19.
[3] Y. Wang, J. Li, H. Zhu, Q. Wang, T. Sun, T. Ni, Y. Lin, Y. Liu, M. Mao, J. Hu, L. Bing, B. B. Hadi, M. Zhongyan, R. Yingjie, S. Feng, T.-N. Ehsan, W. Dawei, S. Kaixin, *Crystals* **2023**, *13*, 1296.
[4] F. F. Wu, D. Zhou, C. Du, B. B. Jin, C. Li, Z. M. Qi, S. Sun, T. Zhou, Q. Li, X. Q. Zhang, *ACS Appl. Mater. Interfaces* **2022**, *14*, 7030.
[5] S. Zhou, Q. Wu, H. Xu, X. Luan, S. Hu, X. Zhou, S. He, X. Wang, H. Zhang, X. Chen, H. Zhou, *Ceram. Int.* **2021**, *47*, 32433.
[6] M. J. S. Rocha, P. M. O. Silva, K. R. B. Theophilo, E. O. Sancho, P. V. L. Paula, M. A. S. Silva, S. B. Honorato, A. S. B. Sombra, *Phys. Scr.* **2012**, *86*, 25701.
[7] H. Zuo, X. Tang, H. Guo, Q. Wang, C. Dai, H. Zhang, H. Su, *Ceram. Int.* **2017**, *43*, 13913.
[8] Z. Yang, Y. Tang, J. Li, W. Fang, J. Ma, A. Yang, L. Liu, L. Fang, *J. Alloys Compd.* **2021**, *867*, 159059.
[9] B. Masin, K. Ashok, H. Sreemoolanadhan, *J. Eur. Ceram. Soc.* **2022**, *42*, 4974.
[10] C. Du, H.-H. Guo, D. Zhou, H.-T. Chen, J. Zhang, W.-F. Liu, J.-Z. Su, H.-W. Liu, *J. Mater. Chem. C* **2020**, *8*, 14880.
[11] M. Haydoura, R. Benzerga, C. L. Paven, L. L. Gendre, V. Laur, A. Chevalier, A. Sharaiha, F. Tessier, F. Cheviré, *J. Alloys Compd.* **2021**, *872*, 159728.
[12] R. F. Abreu, F. R. Silva, S. O. Saturno, D. M. Colares, T. O. Abreu, J. P. C. Nascimento, E. O. Sancho, J. C. Sales, D. X. Gouveia, A. S. B. Sombra, *J. Mechatron. Eng.* **2021**, *4*, 2.
[13] J. D. Bobić, M. M. Vijatović Petrović, J. Banys, B. D. Stojanović, *Mater. Res. Bull.* **2012**, *47*, 18742012.
[14] J. D. Bobić, R. M. Katiliute, M. Ivanov, N. I. Ilić, A. S. Dzunuzović, M. M. Vijatović Petrović, J. Banys, B. D. Stojanović, *J. Alloys Compd.* **2017**, *702*, 619.
[15] J. D. Bobić, M. M. Vijatović Petrović, B. D. Stojanović, *Process. Appl. Ceram.* **2013**, *7*, 97.
[16] Y. Zang, S. Ogurtsov, V. Vasilev, A. A. Kishk, D. Caratelli, *Sensors* **2024**, *24*, 1413.
[17] X. Zhou, L. Liu, J. Sun, N. Zhang, H. Sun, H. Wu, W. Tao, *J. Adv. Ceram.* **2021**, *10*, 778.
[18] A. R. H. Alzakree, C.-H. Wang, M. Shehbaz, W. Wang, D.-M. Xu, C. Du, D. Zhou, *J. Am. Ceram. Soc.* **2024**, *107*, 4738.
[19] A. Zhang, H. Fan, F. Yang, W. Wang, Y. Sun, *J. Alloys Compd.* **2022**, *925*, 166633.
[20] J. Bao, Y. Zhang, H. Kimura, H. Wu, Z. Yue, *J. Adv. Ceram.* **2023**, *12*, 82.
[21] R. F. Abreu, S. O. Saturno, J. P. C. do Nascimento, E. O. Sancho, J. E. V. de Morais, J. C. Sales, D. X. Gouveia, H. D. de Andrade, I. S. Queiroz, A. S. B. Sombra, *J. Electromagn. Waves Appl.* **2020**, *34*, 1705.
[22] L. O. Azevedo, S. J. T. Vasconcelos, H. D. Andrade, I. S. Queiroz Júnior, R. S. Silva, A. S. B. Sombra, *Ceram. Int.* **2021**, *47*, 33232.
[23] H. Tian, J. Zheng, L. Liu, H. Wu, H. Kimura, Y. Lu, Z. Yue, *J. Mater. Sci. Technol.* **2022**, *116*, 121.
[24] T. O. Abreu, R. F. Abreu, F. F. do Carmo, W. V. de Sousa, H. O. Barros, J. E. V. de Morais, J. P. C. do Nascimento, M. A. S. da Silva, S. Trukhanov, A. Trukhanov, L. Panina, C. Singh, A. S. B. Sombra, *Ceram. Int.* **2021**, *47*, 15424.
[25] T. H. de Vasconcelos, H. O. Barros, R. V. B. Campos, F. F. do Carmo, J. P. C. do Nascimento, D. X. Gouveia, M. A. S. Silva, A. J. M. Sales, R. S. Silva, A. S. B. Sombra, *J. Phys. Chem. Solids* **2024**, *184*, 111705.
[26] J. Bao, W. Du, H. Wu, Z. Yue, *J. Am. Ceram. Soc.* **2024**, *107*, 704.
[27] R. F. Abreu, S. O. Saturno, D. M. Colares, F. R. Silva, F. A. C. Nobrega, F. E. A. Nogueira, J. P. C. do Nascimento, S. J. T. Vasconcelos, F. F. do Carmo, T. O. Abreu, A. Ghosh, J. C. Sales, R. S. Silva, A. J. M. Sales, M. A. S. Silva, A. S. B. Sombra, *J. Electron. Mater.* **2023**, *52*, 8050.
[28] F. E. A. Nogueira, T. O. Abreu, V. C. Martins, R. F. Abreu, F. F. do Carmo, J. P. C. do Nascimento, A. Ghosh, A. J. M. Sales, M. A. S. Silva, R. S. Silva, A. S. B. Sombra, *J. Electron. Mater.* **2023**, *52*, 2843.
[29] H. Tian, Y. Zhang, R. Wang, H. Wu, L. Shan, *J. Mater. Sci. Technol.* **2025**, *216*, 165.
[30] H. O. Barros, R. F. Abreu, T. O. Abreu, W. V. de Sousa, F. E. A. Nogueira, F. F. do Carmo, J. E. V. de Morais, J. P. C. do Nascimento, M. A. S. da Silva, R. S. da Silva, S. V. Trukhanov, D. Zhou, C. Singh, A. S. B. Sombra, *Phys. B* **2024**, *695*, 416547.
[31] J. C. Sales, F. A. C. Nobrega, J. P. C. do Nascimento, A. J. M. Sales, W. V. de Souza, F. F. Carmo, R. F. Abreu, M. A. S. Silva, A. S. B. Sombra, *Mater. Today: Proc.* **2024**.
[32] P. M. O. Silva, T. S. M. Fernandes, R. M. G. Oliveira, M. A. S. Silva, A. S. B. Sombra, *Mater. Sci. Eng.: B* **2014**, *182*, 37.
[33] M. P. F. Graça, A. Meireles, C. Nico, M. A. Valente, *J. Alloys Compd.* **2013**, *553*, 177.
[34] B. W. Hakki, P. D. Coleman, *IEEE Trans. Microwave Theory Tech.* **1960**, *8*, 402.
[35] W. E. Courtney, *IEEE Trans. Microwave Theory Tech.* **1970**, *18*, 476.
[36] L. Li, S. Yang, S. Y. Wu, X. M. Chen, *Appl. Phys. Lett.* **2021**, *118*, 212902.
[37] R. K. Mongia, P. Bhartia, *Int. J. Microwave Millimeter-Wave Comput. Aided Eng.* **1994**, *4*, 230.
[38] G. P. Junker, A. A. Kishk, A. W. Glisson, *IEEE Trans. Antennas Propag.* **1994**, *42*, 299598.
[39] J.-F. Kiang, *Novel Technologies for Microwave and Millimeter—Wave Applications*, Springer US, Boston, MA **2004**.
[40] H. M. Rietveld, *J. Appl. Crystallogr.* **1969**, *2*, 65.
[41] H. M. Rietveld, *Acta Crystallogr.* **1967**, *22*, 151.
[42] B. H. Toby, *J. Appl. Crystallogr.* **2001**, *34*, 210.
[43] Y. Bespalko, N. Eremeev, E. Sadovskaya, T. Krieger, O. Bulavchenko, E. Suprun, M. Mikhailenko, M. Korobeynikov, V. Sadykov, *Membranes* **2023**, *13*, 598.
[44] D. Makovec, I. Pribosic, Z. Samardzija, M. Drofenik, *J. Am. Ceram. Soc.* **2001**, *84*, 2702.
[45] I. Pribosic, D. Makovec, M. Drofenik, *J. Eur. Ceram. Soc.* **2001**, *21*, 1327.
[46] P. R. Graves, G. Hua, S. Myhra, J. G. Thompson, *J. Solid-State Chem.* **1995**, *114*, 112.
[47] S. Kojima, R. Imaizumi, S. Hamazaki, M. Takashige, *J. Mol. Struct.* **1995**, *348*, 37.
[48] Z. Z. Lazarevic, N. Z. Romcevic, J. D. Bobic, M. J. Romcevic, Z. Dohcevic-Mitrovic, B. D. Stojanovic, *J. Alloys Compd.* **2009**, *486*, 848.
[49] J. Tellier, P. Boullay, M. Manier, D. Mercurio, *J. Solid State Chem.* **2004**, *177*, 1829.

[50] R. V. Leite, F. O. S. Costa, M. T. Sebastian, A. J. M. Sales, A. S. B. Sombra, *J. Electromagn. Waves Appl.* **2019**, *33*, 84.
[51] J. S. Sarmento, D. V. M. Paiva, E. V. de Araújo, M. A. S. Silva, A. S. B. Sombra, S. E. Mazzetto, P. B. A. Fechine, *Appl. Phys. A* **2023**, *129*, 72.
[52] A. J. Moulson, J. M. Herbert, *Electroceramics: Materials, Properties, Applications*, 1st ed., John Wiley & Sons, Ltd **2003**.
[53] M. T. Sebastian, *Dielectric Materials for Wireless Communication*, Elsevier **2010**.
[54] M. A. S. Silva, R. G. M. Oliveira, A. S. B. Sombra, *Ceram. Int.* **2019**, *45*, 20446.
[55] F. F. Carmo, J. P. C. Nascimento, J. E. V. Morais, V. C. Martins, J. C. Sales, M. A. S. Silva, R. S. Silva, A. S. B. Sombra, *Mater. Chem. Phys.* **2021**, *271*, 124956.
[56] D. M. Colares, R. F. Abreu, F. R. Silva, T. O. Abreu, F. A. C. Nobrega, D. B. Freitas, J. P. C. do Nascimento, F. G. S. Oliveira, I. F. Vasconcelos, A. Ghosh, S. J. T. Vasconcelos, J. C. Sales, R. S. Silva, A. S. B. Sombra, *J. Electromagn. Waves Appl.* **2021**, *36*, 321.
[57] N. D. G. Souza, D. V. M. Paiva, S. E. Mazzetto, M. A. S. Silva, A. S. B. Sombra, P. B. A. Fechine, *J. Electron. Mater.* **2022**, *51*, 761.
[58] C. A. Rodrigues Junior, M. C. Campos Filho, D. G. Sousa, A. J. M. Sales, R. P. S. Leão, A. S. B. Sombra, G. C. Barroso, *J. Electromagn. Waves Appl.* **2018**, *32*, 1329.
[59] V. C. Martins, R. G. M. Oliveira, F. F. Carmo, M. A. S. Silva, S. A. Pereira, J. C. Goes, M. M. Costa, D. X. Gouveia, A. S. B. Sombra, *J. Phys. Chem. Solids* **2019**, *125*, 51.
[60] P. H. T. Silva, M. A. S. Silva, A. S. B. Sombra, P. B. A. Fechine, *J. Mater. Sci.: Mater. Electron.* **2021**, *32*, 18628.
[61] F. A. C. Nobrega, R. F. Abreu, D. M. Co, lares, M. A. S. Silva, F. F. do Carmo, T. O. Abreu, J. P. C. do Nascimento, J. C. Sales, R. S. Silva, J. C. Goes, A. S. B. Sombra, *Mater. Chem. Phys.* **2022**, *289*, 126478.
[62] C. Poole, I. Darwazeh, *Microwave Active Circuit Analysis and Design*, 1st ed., Academic Press **2015**.

